Numerical study of the effects of pod, wand and spike type underdrain systems in pressurized sand filters

Toni Pujol[a], Jaume Puig-Bargués[b], Gerard Arbat[b], Adrián Vegas[a], Miquel Duran-Ros[b], Joan Pujol[b], Francisco Ramírez de Cartagena[b]

[a]Department of Mechanical Engineering and Industrial Construction, University of Girona, c/ Universitat de Girona 4, 17003 Girona, Catalonia, Spain.
[b]Department of Chemical and Agricultural Engineering and Technology, University of Girona, c/ Maria Aurèlia Capmany 61, 17003 Girona, Catalonia, Spain.

Abstract

Commercial sand media filters adopt different underdrain designs, being pod-, wand- and spike-type forms the most common ones. Studies about the consequences of using these configurations are often not conclusive since auxiliary elements and dimensions vary between filters. Here we carried out a numerical analysis of different underdrain designs in filters with equal diffuser plate and same inlet, inner and outlet diameters. Seven underdrain pod-type designs were analysed ranging from a market model to one with more than 50% of pods. Designs with equal number of pods but with different spatial distributions were investigated. Two wand- and two spike-type underdrain models were also evaluated. The main variables analysed were pressure and volumetric flow rate. Results confirmed that the flow uniformity through the filter was crucial to achieve low pressure drop values. The pressure losses through sand became the most important contribution to the filter pressure drop for all cases. The water-only region at the inlet was of low relevance in terms of pressure losses. All underdrain designs had similar pressure drops at the exit collector chamber (pod-type) or pipe (wand- and spike-type). Pod-type designs with the same slot open area than wand- and spike-type configurations clearly had a better efficiency since wand- and spike-type designs had faces opposed to the incoming flow. Pod- and spike-type designs with similar horizontal projected upward slot areas behaved alike in both filtration and backwashing modes, with a better performance for the spike-type configuration. Recommended spike-type designs should cover most of the filter cross-sectional area.

Keywords: Filtration; Granular bed; Drip irrigation; Computational fluid dynamics; Modelling

Highlights:

- The hydraulic performance of different underdrain type designs was assessed.
- Pod-, wand- and spike-type underdrains designs were studied.
- Flow uniformity in sand media was crucial to reduce pressure losses.
- Similar performance of different designs with equal projected horizontal upward slot areas.
- Spike-type designs should cover most of the filter cross-sectional area.

Nomenclature

A	Cross-sectional area of the filter tank (m^2)
A_c	Horizontal area covered by the underdrain system (m^2)
A_e	Total exit area of an underdrain unit (m^2)
A_o	Total slot open area (m^2)
A_{oh}	Horizontal projection of the total slot open area (m^2)
$A_{s,i}$	Horizontal area served per underdrain (m^2)
$\overline{A_s}$	Average horizontal area served by underdrain (m^2)
$A1, \cdots, A10$	Inner circular area (m^2)
c_v	Coefficient of variation of the horizontal area served per underdrain unit (dimensionless)
C_2	Inertial resistance factor of the granular bed (m^{-1})
d_{10}	Sand effective diameter (mm)
H_s	Height of the sand column (mm)
N	Number of underdrain units (dimensionless)
P	Pod-type underdrain (-)
RANS	Reynolds-averaged Navier-Stokes (-)
S	Spike-type underdrain (-)
Q	Volumetric flow rate ($m^3\ h^{-1}$)
v	Flow velocity ($m\ s^{-1}$)
v_s	Superficial velocity ($m\ h^{-1}$)
W	Wand-type underdrain (-)
z	Total height (m)

α Permeability of the granular bed (m^2)

Δp_f Pressure drop through the filter in filtration mode (kPa)

$\Delta p_{f,id}$ Pressure drop through the ideal filter case in filtration mode (kPa)

$\Delta p_{f,w}$ Pressure drop through the filter without sand media in filtration mode (kPa)

$\Delta p_{b,w}$ Pressure drop through the filter without sand media in backwashing mode (kPa)

μ Fluid viscosity (Pa s)

ρ Fluid density (kg m^{-3})

σ_s Standard deviation of the $A_{s,i}$ dataset (m^2)

∇p Pressure gradient (Pa m^{-1})

Subscripts

i i-th underdrain unit (dimensionless)

1. Introduction

Pressurized sand media filters are widely used in drip irrigation systems. They are intended to remove large particles carried by irrigation water, allowing the particle load to be in the range that emitters and distribution system can tolerate for long operational periods (Nakayama, Boman, Pitts, 2007). In filtration mode, low quality water is forced to flow through the granular bed contained in a closed tank (Mesquita, Testezlaf, Ramirez, 2012). Solid retention mainly occurs in the upper layers of the filtration bed since the typical dimension of the free passage through sand pores is smaller than that of suspended particles (Ojha & Graham, 1994). , Filter pressure drop increases as particles accumulate in the first layers of the granular bed. This implies that filtration velocity is most important than sand media height in order to develop clogging conditions (Solé-Torres et al., 2019). In backwashing mode, valves revert the flow normal direction so as to suspend the sand particles inside the closed tank. This process releases the solids retained in the sand during the filtration mode, being transported out of the system by the reverse water stream (de Deus, Mesquita, Salcedo Ramirez, Testezlaf, de Almeida, 2020). This fluidized bed regime requires a higher inlet pressure than that of the filtration mode in order to achieve the recommended backwash flow rate.

Several studies have aimed to increase the efficiency of filters by focusing on reducing the overall pressure drop (e.g., Bové et al., 2015a). This goal can be accomplished by improving the design of the main elements of the filter: diffuser plate, underdrain and collector. The diffuser plate is located at the entrance of the closed tank to reduce the water momentum and to uniformise the flow inside it (Mesquita, de Deus, Testezlaf, da Rosa, Diotto, 2019). The underdrain allows water to pass through it but not sand. The underdrain uses a system with slots of characteristic width smaller than the grain size of the granular bed (Bové et al., 2015b). Finally, the collector is the element in charge of collecting clean water at the underdrain exit and of directing it towards the exit pipe.

Commercial filters use a wide variety of underdrain designs. The most common ones can be classified as: pods, wands and spikes. Pods are of either cylindrical or truncated conical shapes, with vertically oriented slots along its surface of revolution. Multiple pods are located in a plate at the bottom of the sand column (see, e.g., Arbat et al., 2013). Wands are cylindrical elements with longitudinal slots whose axis of revolution is horizontal. Multiple wands are located in parallel, being connected to a central pipe that acts as an exit collector (Pujol et al., 2020). Finally, spike designs use horizontal cylindrical elements similar to those of wands but distributed in a radial form. These spikes are joined to a drainage pipe located at the filter centre (Burt, 2010).

Burt (2010) experimentally studied five commercial models of sand media filters with different underdrain designs operating at different flow rates for both filtration and backwashing modes. He found that wand type as well as hybrid spike-pod type (pods located in radial arms) underdrains generated the less pressure drop in the sand medium for both filtration and backwashing modes. Burt (2010) also observed high pressure drops through some of the three-way valves used to change the filter operational mode. The pressure drop through these external valves was even higher than that due to the granular bed in some commercial filters.

Mesquita, Testezlaf and Ramirez (2012) focused on the effect of internal auxiliary elements on the filter pressure drop. They found that head losses were substantially affected by the internal elements, so changes in their designs led to large variations in the filter total pressure drop. More recently, Mesquita et al. (2019) improved the design of the diffuser plate of a commercial filter by means of a numerical model. The new design was able to reduce the vortex at the upper filter chamber, which minimized the deformation of the upper sand layer and increased the flow uniformity. This effect diminished the probability of having preferential paths within the media.

As Burt (2010) already pointed out, the horizontal area served by commercial underdrains is small in comparison with the cross-sectional area of the filter. This indicates the existence of changes in the flow direction inside the granular bed (and, likely, of flow convergences) that can cause additional increase of head losses. Arbat et al. (2011) confirmed the narrowing of the streamlines as flow approached the slots of the pods in a numerical analysis of a commercial filter. This increase of the flow speed inside the sand implied a substantial raise in the pressure drop. Pujol et al. (2016) experimentally analysed a modified commercial pod in order to diminish the region of sand affected by the underdrain. They obtained filter pressure drop reductions of 20% and 25% by redistributing and increasing the number of slots, respectively. Bové et al. (2017), numerically, and Carles-Solé et al. (2019), experimentally, analysed a prototype of underdrain with a total slot open area equal to that of the filter's cross-section. In comparison with commercial filters working under the same conditions of sand height and flow rate, the new design achieved better turbidity removals, increased the filtered volume per filtration cycle and reduced the electrical energy consumption.

Related to the slot open area, it is expected that underdrain designs with slots facing towards the incoming flow will work better than those placed in other orientations. This effect was quantitatively analysed by Pujol et al. (2020) in the numerical study of a commercial filter with wand-type underdrains. They found that those slots in a wand that were facing towards the bottom of the filter (i.e., opposing to the incoming flow), contributed less than 40% to the volume of filtered water. They slightly improved this contribution by redistributing the wands so as to serve the same horizontal surface area.

Commercial filters that use different underdrain designs also differ in other geometrical features, like tank dimensions, diffuser plate design, etc. Therefore, the comparison of commercial filters makes difficult to draw conclusions on the particular effect of the underdrain design. The purpose of the present work was to overcome this difficulty by analysing several configurations of the underdrain (pods, wands and spikes) when installed in a filter with the same dimensions, equal diffuser plate and working under the same conditions of sand media heights and flow rates. The study was carried out numerically since it allowed the development of more designs (11 underdrains divided into: 7 pod-type, 2 wand-type and 2 spike-type) with a very detailed information of the key variables involved in the process. In particular, we were interested in the pressure drop and flow uniformity in the different filter zones as well as their relationships with the area served per underdrain element and the total slot open area.

2. Materials and methods

2.1 Filter designs

The sand media filters analysed were based on the commercial model FA1M (Lama, Gelves, Spain). This filter uses wand-type underdrains and its hydraulic performance was numerically studied in Pujol et al. (2020). Inner diameters of both inlet and outlet pipes were 40.80 mm. The inner diameter of the cylindrical body of the pressurized tank was 500 mm. Upper and lower shapes of the pressurized tank were spherical with radius 500 mm. The diffuser plate was a circular element of 120 mm diameter located inside the tank at 50 mm from the flow entrance. It was held by four equally distributed plates, 3 mm wide and 37 mm long, welded to the tank. The previous elements and dimensions were kept equal for all the filters analysed. These were divided into three categories: a) pod-type underdrains; b) wand-type underdrains and c) spike-type underdrains (see Fig. 1). In comparison with wand- and spike-type filters, those with pod-type underdrains required a bottom chamber in order to collect the water discharged through these elements (see, e.g., Arbat et al., 2011 and Fig. 1). In contrast, wand- and spike-type filters employed collector pipes to flush clean water out of the system. Thus, the height of the tank cylindrical body was 400 mm for wand, spike and upper chamber of pod-type underdrain filters and 150 mm for the lower chamber of pod-type underdrain filters.

Pod-type underdrains were of truncated conical shape installed in a horizontal plate at the base of the upper filter chamber (see, e.g., Fig. 1). These elements were based on commercial units (Regaber, Parets del Vallès, Spain) analysed in previous studies (e.g., Pujol et al., 2016), although slightly modified for the numerical analysis. The upper part of the pods was flat and the outer reinforcement ring was removed. The inner shape of the pods was kept equal as in the commercial unit since we were interested in finding the head losses through this element (see Fig. 2A). Each pod consisted of 45 trapezoidal slots of width ranging from 0.44 to 0.47 mm and length 26.43 mm with a total area per slot equal to 12.06 mm^2. The total open area of a pod was 542.93 mm^2. Water flowing through the pod entered into the lower filter chamber with a conduit 21 mm long with 16 mm diameter.

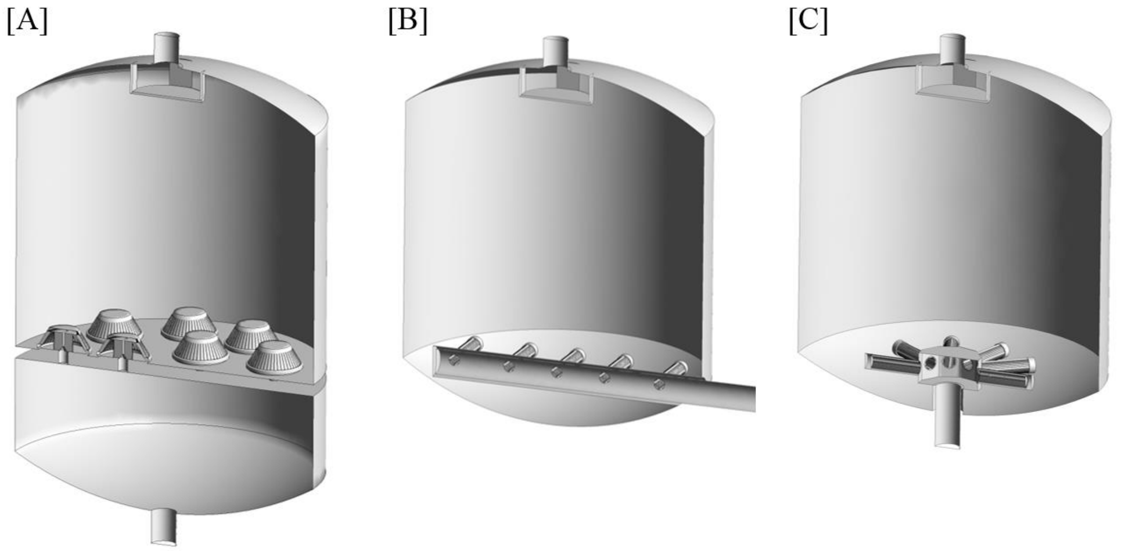

Fig. 1 – Example of cross-sectional views of some [A] pod-type, [B] wand-type and [C] spike-type underdrains analysed in the present study.

Wand-type underdrains followed those studied in Pujol et al. (2000) (see Fig. 2). Essentially, each wand had 24 rectangular slots of dimensions 0.51×79 mm^2 (= 40 mm^2). The total open area per wand was 960 mm^2. Wands were located in parallel to each other, and all wands were connected through a circular section of 284 mm^2 to a horizontal collector pipe of 40.80 mm diameter. The two designs of wand-type filters here analysed used the same type of underdrain element since only differed in the horizontal separation between them. The spike-type underdrains here tested were based on the previous wand geometry. Dimensions and total open area per spike were equal to those per wand (i.e., total open area of 960 mm^2 per spike). The main difference in comparison with the wand-type filters was the radial distribution of the spikes (see Fig. 1C). Clean water inside the spikes flowed towards a central collector that had a vertical exit pipe of 40.80 mm diameter and 100 mm length. The two designs of spike-type filters here analysed varied in the length of the radial spikes although they had the same slot open area. The first design shown in Fig. 1C exactly reproduced the geometry of wands in Fig. 2B. In the second design, the longitudinal slots were cut in two parts so the spike was longer though equal in terms of open area (see Fig. 2C).

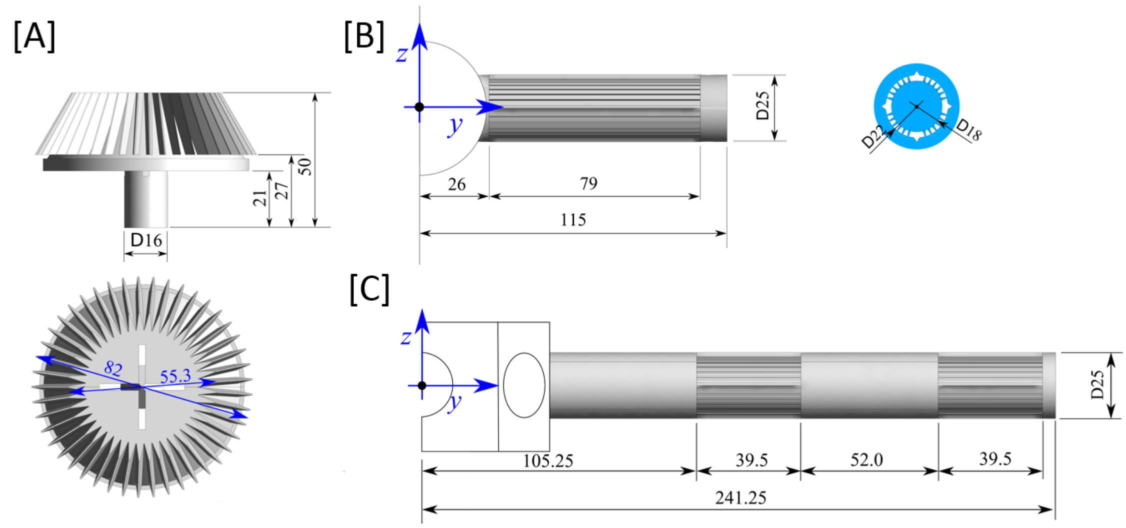

Fig. 2 – Main dimensions of [A] the inner volume of a pod, [B] wand underdrain, and [C] spike (type b) underdrain in which the cross-sectional area is equal to that shown in blue in [B]. Units in mm.

A total of twelve underdrain designs were investigated in the present study (see Fig. 3). Table 1 summarises their main geometrical parameters, some of them based on those introduced by Burt (2010). The average horizontal area served by each underdrain unit $\overline{A_s}$ followed

$$\overline{A_s} = \frac{A}{N} \quad (1)$$

where A was the cross-sectional area of the tank and N the number of underdrain units employed (i.e., number of pods, wands or spikes).

The coefficient of variation of the horizontal area served per underdrain unit c_v was calculated from

$$c_v = \frac{\sigma_s}{\overline{A_s}} \quad (2)$$

where σ_s was the standard deviation of the set of values formed by the horizontal area served per underdrain $A_{s,i}$ (with i the i-th underdrain unit). Note that $A = \sum_{i=1}^{N} A_{s,i}$. Values of $A_{s,i}$ were estimated by dividing the filter cross-sectional area into different regions surrounding each underdrain unit. For doing so, sketches for each one of the filter designs were made similar to those presented in Burt (2010). For pod-type designs, the patterns arose after drawing lines perpendicular to the segments that united two neighbour pods and that crossed the mid-point of these segments. For wand-type designs, patterns were similar to those shown in Pujol et al. (2020). Finally, for spike-type ones, patterns were circular sectors in the case shown in Fig. 1C and circular plus annular sectors when using the underdrain shown in Fig. 2C. In the latter case, circular and annular sectors had the same surface area since the two discontinuous segments of slots in the spike were located at the middle of these sectors.

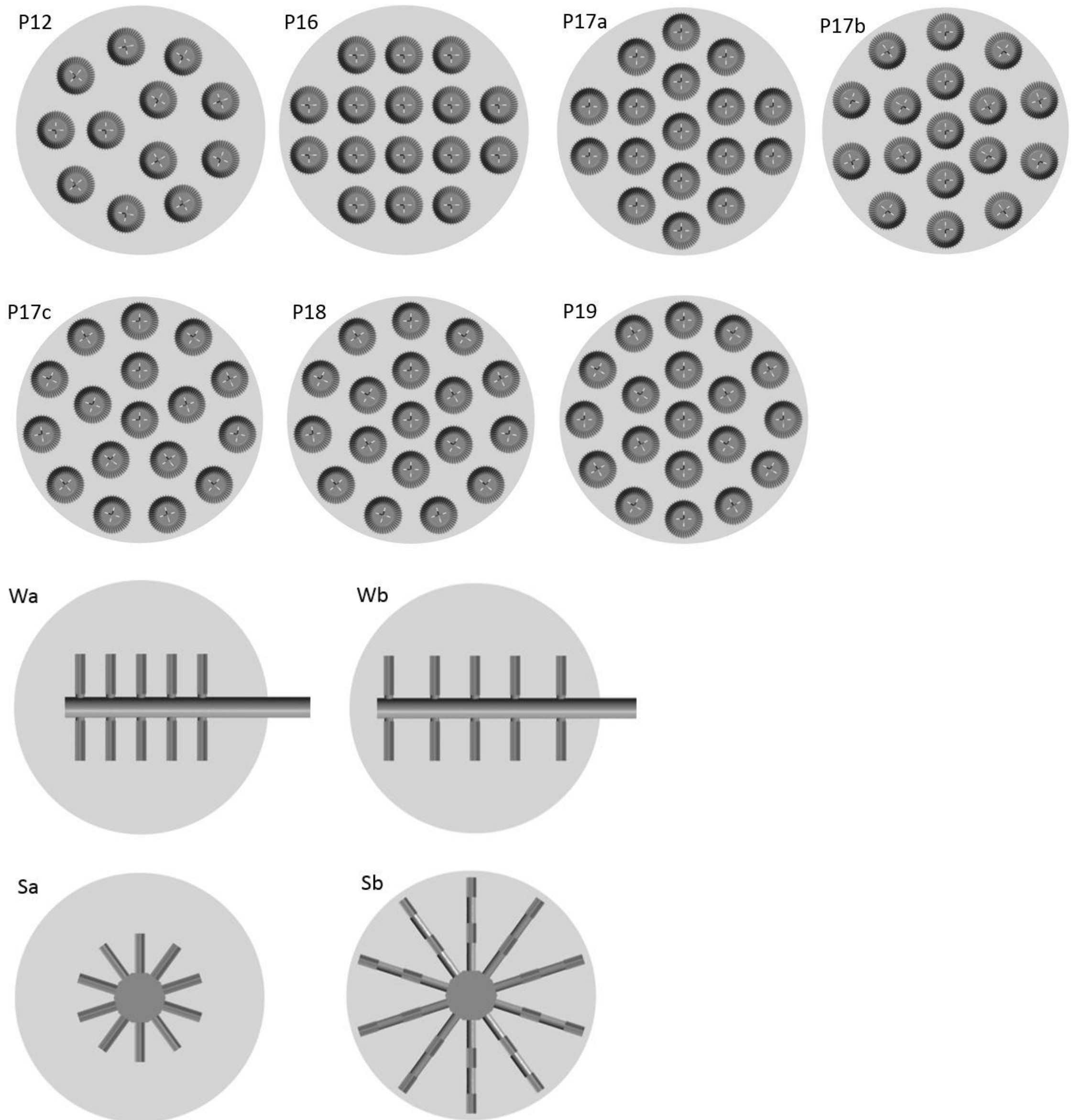

Fig. 3 – Underdrain configurations analysed in the present study. Pod-type underdrains (P12 to P19, the number states the pods in each configuration), wand-type underdrains (Wa to Wb) and spike-type underdrains (Sa to Sb). An additional ideal case with slot open area equal to that of the base plate in pod-type filters was also analysed (i.e., case without underdrain element). Base plate diameter was 0.50 m. See the supplementary material for a detailed description of the geometrical configurations.

Table 1 also shows values of total slot open area A_o and its horizontal projection A_{oh}. In the latter case, only slots facing towards the incoming flow were taken into account. This included all slots for pod-type underdrains and only half of the slots for wand- and spike-type ones. On the other hand, the exit area from the underdrain system A_e (i.e., the cross-sectional area of the underdrain that connected with the lower filter chamber in pod-type underdrains or with the collector pipe in wand- and spike-type ones) was also reported. Finally, Table 1 includes the horizontal projection of the whole underdrain system (covered area A_c). The last row in Table 1 corresponds to an ideal design in which the underdrain system was the whole cross-sectional area of the filter. Although this design is unrealistic, since the sand column must be held by a physical element, it was simulated so as to provide the ideal solution.

Table 1. Average horizontal area served per underdrain unit $\overline{A_s}$, coefficient of variation c_v, total slot open area A_o, horizontal projection of the total slot open area A_{oh}, total exit area of the underdrain units A_e, and horizontal area covered by the underdrain system A_c, for all the filter designs here analysed (see Fig. 3).

Underdrain design	$\overline{A_s}$ ($\times 10^{-4}$ m^2)	c_v	A_o ($\times 10^{-4}$ m^2)	A_{oh} ($\times 10^{-4}$ m^2)	A_e ($\times 10^{-4}$ m^2)	A_c ($\times 10^{-4}$ m^2)
P12	163.63	0.11	65.15	32.95	24.13	729.85
P16	122.72	0.22	86.87	43.93	32.17	973.14
P17a	115.50	0.23	92.30	46.68	34.18	1033.96
P17b	115.50	0.16	92.30	46.68	34.18	1033.96
P17c	115.50	0.08	92.30	46.68	34.18	1033.96
P18	109.08	0.09	97.73	49.42	36.19	1094.78
P19	103.34	0.10	103.16	52.17	38.20	1155.60
Wa	196.35	0.35	96.01	32.01	26.13	449.00
Wb	196.35	0	96.01	32.01	26.13	450.00
Sa	196.35	0	96.01	32.01	26.13	301.97
Sb	196.35	0	96.01	32.01	25.45	558.95

Ideal	1963.50	0	1963.50	1963.50	1963.50	1963.50

2.2 Numerical model

The numerical model was developed with ANSYS-Fluent. This commercial tool has previously been applied to simulate the behaviour of pressurized sand media filters with successful results (e.g., Arbat et al., 2011; Bové et al., 2017; Pujol et al., 2020). It is based on the finite volume method, which is used to solve the fluid dynamics governing equations (ANSYS, 2017). For all cases, we made use of symmetry conditions through the vertical plane and only half of the filter was simulated (i.e., as images shown in Fig. 1). This half-filter domain was divided into three different bodies. Both entry and underdrain plus collector zones were defined as only water regions. A domain located in the middle, between the entry regionand the underdrain, was defined as a porous zone. In this domain, an additional head loss due to the effect of sand was added to the momentum equation. This was based on the Ergun equation, being

$$-\nabla p = \frac{1}{\alpha}\mu v_j + C_2 \frac{\rho}{2}|v|v_j \quad for\ j = x, y, z \tag{3}$$

where ∇p was the pressure gradient, v_j was the j-th component of the flow velocity, $|v|$ was the magnitude of the flow velocity, μ (= 10.03×10^{-4}Pa s) was the fluid absolute viscosity, ρ (= 998.20 kg m^{-3}) was the fluid density, and $1/\alpha$ (= 5.60×10^{9} m^{-2}) and C_2 (= 0 m^{-1}) were the inverse of the permeability and the inertial resistance factor of the granular bed, respectively. These values of α and C_2 were chosen equal to those obtained in Pujol et al. (2020), who experimentally and numerically analysed a wand-type commercial filter (Wa case in Fig. 3) working with silica sand of d_{10} = 0.48 mm effective diameter and 38.50×10^{-2} porosity. They calibrated both α and C_2 parameters of the same numerical model as the one here employed (Wa case) by minimising the error between simulated and measured filter pressure drops at different flow regimes and sand media heights. The above values of $1/\alpha$ and C_2 gave a root mean square relative error lower than 1.9% with a maximum error in the data series lower than 2.3% (Pujol et al., 2020).

Eight different operational conditions were simulated for each one of the 12 underdrain configurations plus ideal case listed in Table 1 (see Table 2). The filtration mode was analysed without granular bed, and with two different heights of sand H_s (= 162.50 mm and 300 mm) measured from a reference level defined as the middle vertical position of the slots in an underdrain element. For pod-type designs, the reference level was 19 mm above the underdrain base plate (we point out that the pod cover whose bottom side was in contact with the base plate and the upper side was in contact with the inner volume shown in Fig. 2A was 1.50 mm wide). This meant sand heights of 181.50 mm and 319 mm above the bottom plate of the upper chamber (Fig. 1A). In contrast, the reference level to measure H_s for both wand- and spike-type designs was that defined by the horizontal axis of the cylindrical underdrains (Fig. 1B-C). The backwashing regime was investigated for the water-only situation case since the methodology applied to take the granular bed into account did not assume the movement of sand grains. Two different values of volumetric flow rate were investigated Q = 6 m^3 h^{-1} and Q = 12 m^3 h^{-1} that corresponded to superficial velocities v_s (volumetric flow rate divided by cross-sectional area of the filter tank) of 30.56 m h^{-1} and 61.12 m h^{-1}, respectively. Working conditions recommended by the manufacturers for these types of filters would correspond to those of high column of granular bed (H_s = 300 mm) and superficial velocities on the order of 61.12 m h^{-1} (see, e.g., Solé-Torres, 2020). However, filtration with lower superficial velocities (e.g., 20 m h^{-1}) in commercial sand filters have been also investigated (Mesquita et al., 2012). Therefore, the flow rate values here analysed represented quite well the range of common operational conditions of these types of filters.

Table 2. Operational conditions simulated for filtration and backwashing modes. H_s is the height of the sand column calculated from the underdrain centreline. Q is the volumetric flow rate.

	Water-only	H_s = 162.50 mm	H_s = 300 mm
Q = 6 m^3 h^{-1}	Filtration/Backwashing	Filtration	Filtration
Q = 12 m^3 h^{-1}	Filtration/Backwashing	Filtration	Filtration

Steady state simulations were carried out. The pressure-based solver with the coupled algorithm for the pressure-velocity coupling was chosen. The discretization scheme was of second-order for all variables. Boundary conditions were constant pressure (= 210 kPa, relative) at the inlet and constant velocity (equal to volumetric flow rate divided by the surface area) at the outlet. Walls were assumed non-slip and smooth. The Reynolds-averaged Navier-Stokes (RANS) methodology to deal with the turbulence flow was chosen. The closure of the momentum equations was done with the shear stress transport (SST) k-ω two-equation eddy-viscosity model, in which k was the turbulence kinetic energy and ω was the specific dissipation rate of turbulence kinetic energy. This model applies the k-ω formulation in the inner parts of the boundary layer, being very suitable for low Reynolds scenarios (as expected in the granular bed region) and shifts to the k-ε in free-stream conditions, where ε is the dissipation rate of turbulence kinetic energy. A turbulent viscosity ratio of 10% and a turbulence intensity of 5% were set at both inlet and outlet boundaries. The acceleration of gravity was taken into account.

Tetrahedrons were used to discretise the domain, with five layers of prisms attached to the inner filter walls to better capture the boundary layer. The maximum size of the elements was 0.80 mm at underdrain walls, 0.30 mm at slots, 3 mm in the diffuser plate and at both inlet and outlet pipes, and 10 mm inside the domains (limited to a maximum of 3 mm inside the underdrain domains). The growth factor was fixed to 20%. For the P17b case, for example, this configuration required a total amount of 18.49×10^{6} elements to discretise half of the filter (see Fig. 4). For these meshes the maximum skewness factor was below 0.88, the maximum aspect ratio below 16.08 and the minimum orthogonal quality was above 0.12. Finer and coarser meshes were also developed to determine the sensitivity of the results to the mesh dimensions, as explained later. The mesh configuration followed that employed in Pujol et al., 2020.

The maximum value of the residuals was set to 10^{-5} for all the variables. However, simulations ran a minimum of 150 iterations after the residual convergence criterion was reached. The values of the reported variables corresponded to the averages of the last 150 iterations. In all cases, we monitored the imbalance between the inlet and the outlet mass flows and these were below 0.02%.

A sensitivity study was carried out by modifying the turbulence model, by assuming non-smooth surfaces and by increasing the number of prism layers to 10 in the inflation zone. For the P17b case with H_s = 162.50 mm and Q = 6 m^3 h^{-1}, the variation of the pressure drop through the filter Δp_f increased 0.20% when using the realizable k-ε turbulence model instead of the SST k-ω. A similar increase of 0.19% was obtained when using 10 layers of prisms in the inflation zone. Finally, an increase of 0.05% in Δp_f was found when defining all inner filter walls as steel made with a value of the absolute surface roughness equal to 0.10 mm and all underdrain elements as polyvinyl chloride (PVC) made with a value of the absolute surface roughness equal to 15×10^{-4} mm.

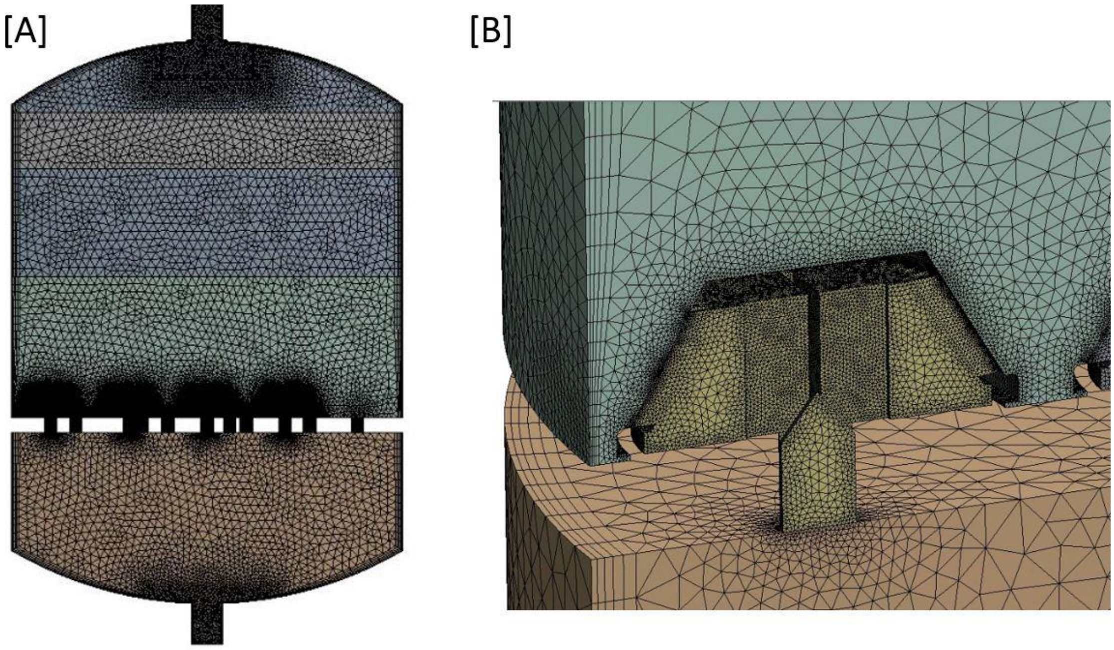

Fig. 4 – Mesh at the symmetry plane [A] and detail of one pod [B] for the P19 case.

On the other hand, we carried out a mesh sensitivity study for the P17b case. The characteristic values of the mesh size described above were multiplied by a factor of 0.66, 0.83, 1.33 and 1.50, respectively. The meshes obtained had a number of elements equal to 36.42×10^6, 26.95×10^6, 11.59×10^6 and 8.79×10^6, respectively, for discretising half of the filter. Results of the filter pressure drop Δp_f obtained with the H_s = 162.50 mm and Q = 6 m^3 h^{-1} operational conditions are shown in Fig. 5. Note that pressure drop with the 18.49×10^6 elements case differed less than 0.07% with respect to that of the finer mesh. Coarser discretisations (11.59×10^6 and 8.79×10^6) gave differences above 0.30% in comparison with the output result of the finer mesh. Therefore, the discretisation of the mesh with 18.49×10^6 elements was assumed to be good enough for our study. The small variation of the results observed with respect to finer meshes supported the robustness of the conclusions extracted from our numerical comparative analysis. For completeness, we note that a similar mesh sensitivity study was done for the wand-type underdrain filters in Pujol et al. (2020).

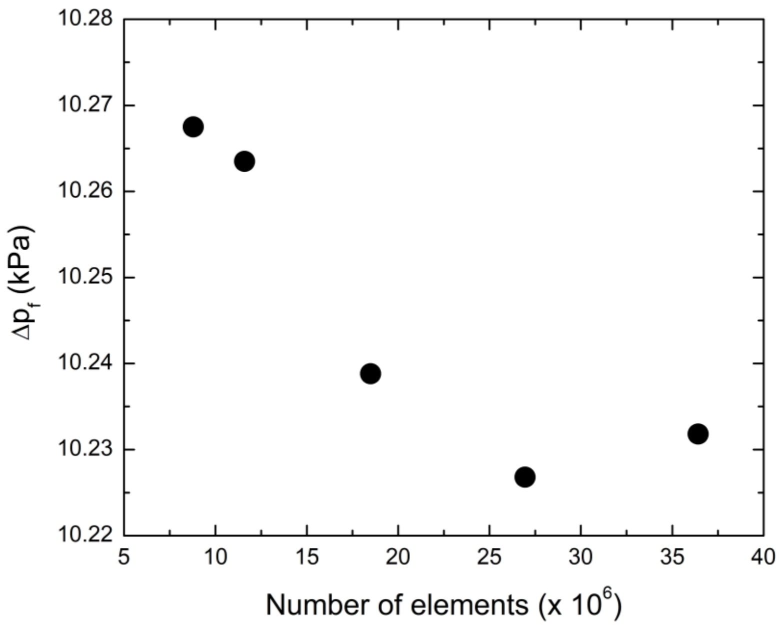

Fig. 5 – Filter pressure drop for case P17b with H_s = 162.50 mm, Q = 6 m^3 h^{-1} obtained when using different mesh sizes.

3. Results and discussion

3.1 Filtration mode

3.1.1 Filter pressure drop as a function of underdrain design

Values of filter pressure drop for the operational conditions listed in Table 2 are shown in Figure 6. As expected, for a given filter design, the maximum pressure drop occurred with the highest flow rate (= 12 m^3 h^{-1}) and sand media column (300 mm) (Fig. 6A). For pod-type underdrain designs, the filter head loss ranged from 39.5 kPa (P12) to 36.2 kPa (P19). Larger variations were found for the spike-type design, with 44.4 kPa and 38.8 kPa for the Sa and Sb configurations, respectively. The pressure drop value for the ideal case was used to calculate the ratio $\Delta p_f/\Delta p_{f,id}$, employed to determine how close to the ideal conditions the system was (see Fig. 6B). For the P19 design, $\Delta p_f/\Delta p_{f,id}$ < 1.04 for all operational conditions. However, this ratio increased up to 1.18 for the P12 design (which was the pod-type underdrain design closest to a commercial model), indicating that there was still room for improvement. The P12 and the Sb designs behaved similarly. Wand-type and spike-type, version Sa, were substantially far from the ideal filter pressure drop values. -In general, for a constant value of sand height, the $\Delta p_f/\Delta p_{f,id}$ value increased as flow rate increased. This occurred by the convergence of the flow streamlines as they approached the slots of the underdrains within the sand zone. As expected, this effect diminished in designs with larger total slot open area A_0. The Sa design was the exception to this behaviour since even at low flow rates, the curvature of the streamlines was very important there. For a constant value of flow rate, the $\Delta p_f/\Delta p_{f,id}$ value reduced as sand height increased since the local effect of the underdrains became less relevant to the total filter pressure drop.

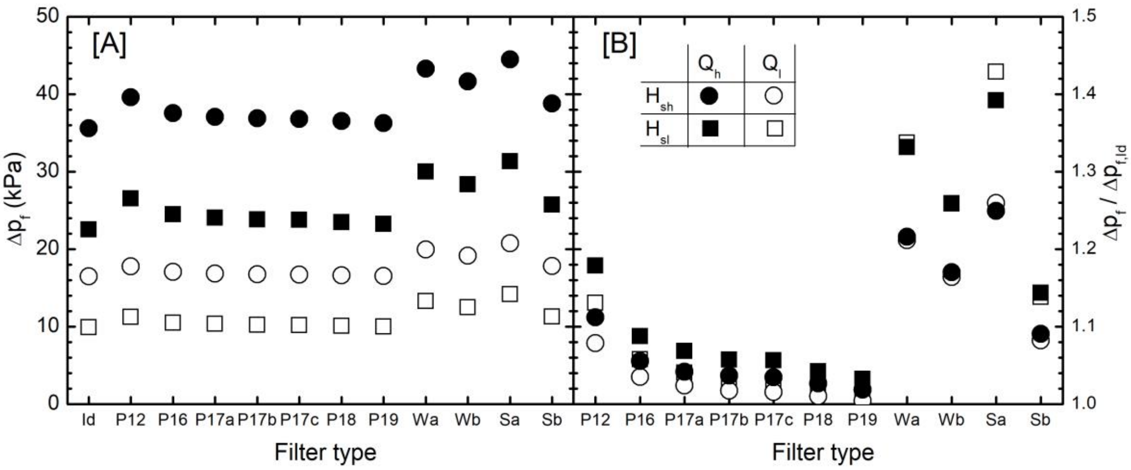

Fig. 6 – Filter pressure drop for filters with different underdrain designs [A] and ratio of filter pressure drop to that of the ideal case [B] as a function of sand media height and volumetric flow rate. H_{sh} = 300 mm, H_{sl} = 162.50 mm, Q_h= 12 m^3 h^{-1}, Q_l = 6 m^3 h^{-1}.

3.1.2 Filter pressure drop as a function of geometrical parameters

The $\Delta p_f/\Delta p_{f,id}$ ratio as a function of the percentage of the cross-sectional area occupied by the slot projected area A_{oh} is shown in Fig. 7A. A very large variation of the $\Delta p_f/\Delta p_{f,id}$ ratio was found at the lowest A_{oh} value since it corresponded to all wand- and spike-type designs (see Table 1). The filter pressure drop tended to the ideal condition (i.e., $\Delta p_f/\Delta p_{f,id}$ = 1) as the slot projected area increased. A somehow apparent trend was also observed between $\Delta p_f/\Delta p_{f,id}$ and the percentage of the cross-sectional area of the filter occupied by the underdrain system A_c (see Fig. 7B). A priori, there should not be a clear relationship between both terms since equal values of A_c could have very different values of slot open areas. However, unfeasible commercial designs were not investigated here (e.g., high A_c with small A_o), so it is likely that the tendency obtained in Fig. 7B applies to those pressurized sand media filters close to market.

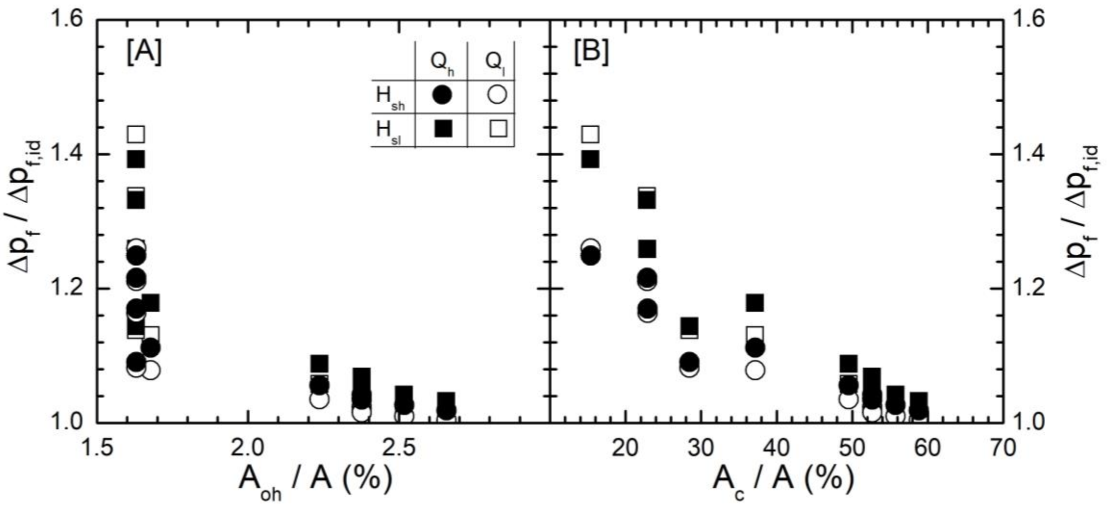

Fig. 7 –Ratio of filter pressure drop to that of the ideal case as a function of the percentage of filter cross-sectional area occupied by [A] the slot projected area A_{oh} and [B] the underdrain system A_c. H_{sh} = 300 mm, H_{sl} = 162.50 mm, Q_h= 12 m^3 h^{-1}, Q_l = 6 m^3 h^{-1}.

For a given design, all data collapsed into a single point when applying the formula $(\Delta p_f - \Delta p_{f,w} - \Delta p_{s,id})/v_s$, with $\Delta p_{s,id}$ the ideal pressure drop of a sand column with a height equal to that used in the filter (i.e., pressure drop in a cylinder with height of sand H_s). The term $\Delta p_f - \Delta p_w$ can be understood as the pressure drop in the sand region. Therefore, the term $\Delta p_f - \Delta p_w - \Delta p_{s,id}$ is an estimate of the pressure drop due to the effect of the underdrain only. Since pressure drop in the sand was a linear function of superficial velocity (see Eq. (3)), the $(\Delta p_f - \Delta p_w - \Delta p_{s,id})/v_S$ term quantitatively reported the relevance of the underdrain design. Figure 8 shows this term as a function of the percentage of the average horizontal area served per underdrain with respect to the total filter horizontal area $(\overline{A_s}/A)$.

As pointed out above, all working points for a given design almost led to the same value. The four set of points shown at $\overline{A_s}/A$ = 10% corresponded to Sa, Sb, Wa and Wb cases, with Sa having the highest value and Sb the lowest one. As expected, there was a growing trend of the underdrain relevance as $\overline{A_s}/A$ increased, with the Sb case being clearly aligned with the almost linear behaviour observed for the pod-type designs. This revealed that the long spike-type design was comparable to pod-type ones. Wand-type and, especially, short spike-type designs had a higher underdrain influence on the pressure drop than that expected for equivalent pod-type models.

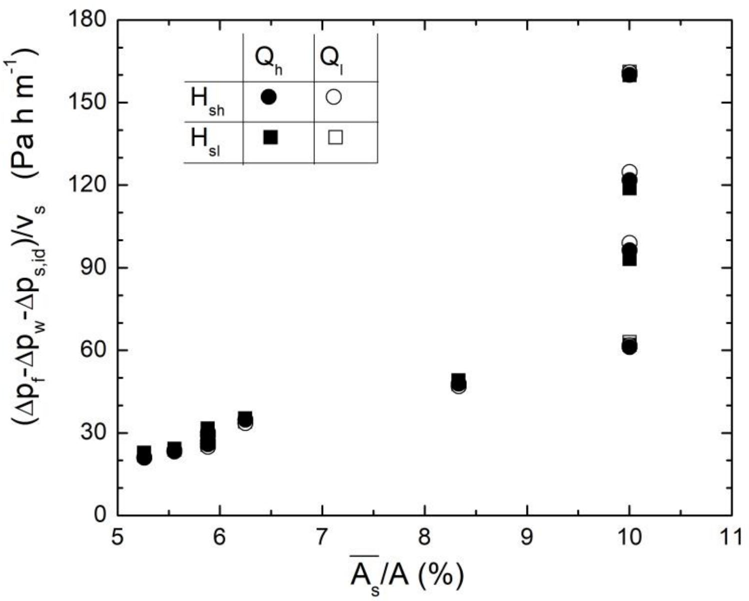

Fig. 8 –Estimate of the pressure drop due to the influence of the underdrain divided by the superficial velocity as a function of the ratio between the average horizontal area served per underdrain and the filter horizontal area (in percentage). Data per each filter design collapse into a single value. H_{sh} = 300 mm, H_{sl} = 162.50 mm, Q_h= 12 m^3 h^{-1}, Q_l = 6 m^3 h^{-1}.

3.1.3 Pressure vertical profiles

Figure 9 shows the area averaged (xy-plane) values of pressure for different pod-type designs as well as for the ideal case (without underdrain) for $H_s = 300$ mm and $Q = 12$ m^3 h^{-1}. Note that pressure within the sand region of the ideal case followed a line with a slope equal to the right-hand side of Eq. (3).

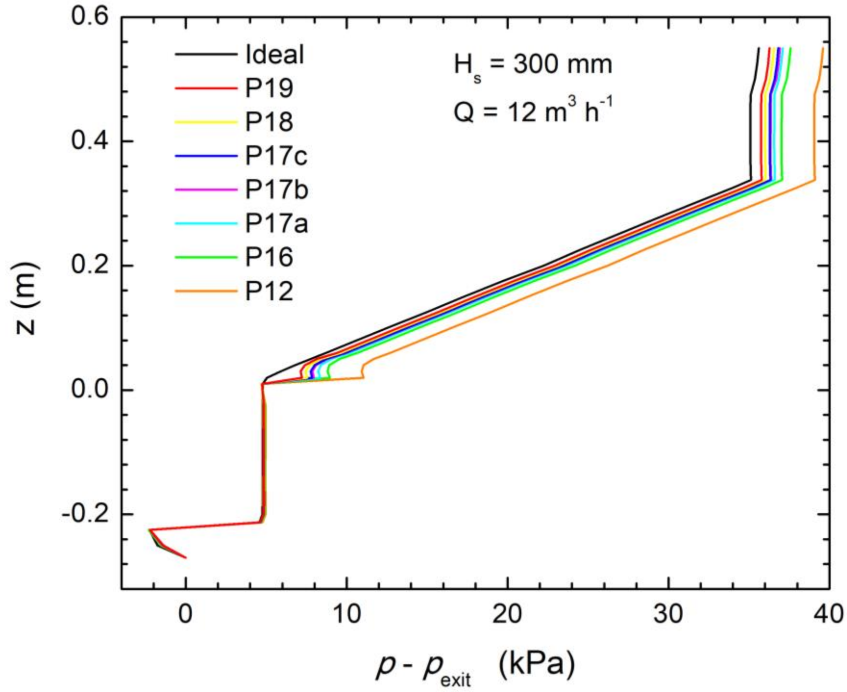

Fig. 9 – Vertical profile of the area averaged (xy-plane) pressure difference with respect to the exit value for pod-type underdrain designs and an ideal case without underdrain for operational conditions H_s = 300 mm and Q = 12 m^3 h^{-1}.

The same slope within the sand was observed for all pod-type designs except in a region close to the underdrain (see Fig. 9). Below $z < 0.06$ m, values of the area averaged (xy-plane) pressure slightly varied, indicating that constant pressure surfaces deviated from the horizontal plane. An abrupt decrease of the average value of pressure was observed in the $0 < z < 0.01$ m region due to the underdrain effect.. Note that, in pod-type underdrains, pressure variations were almost null at the collector chamber and, also, in the upper water-only chamber below the diffuser plate. The effect of the diffuser plate and, especially, of the contraction zone at the filter exit were more relevant.

Local values of pressure along several lines are shown in Fig. 10, where we also represent pressure contours in a vertical plane located at x = 0 m. The range of pressure contours depicted is limited to 170 – 190 kPa for a better clarity of their behaviours near the underdrains. The operational conditions were equal than in Fig. 9 ($H_s = 300$ mm and $Q = 12$ m^3 h^{-1}).

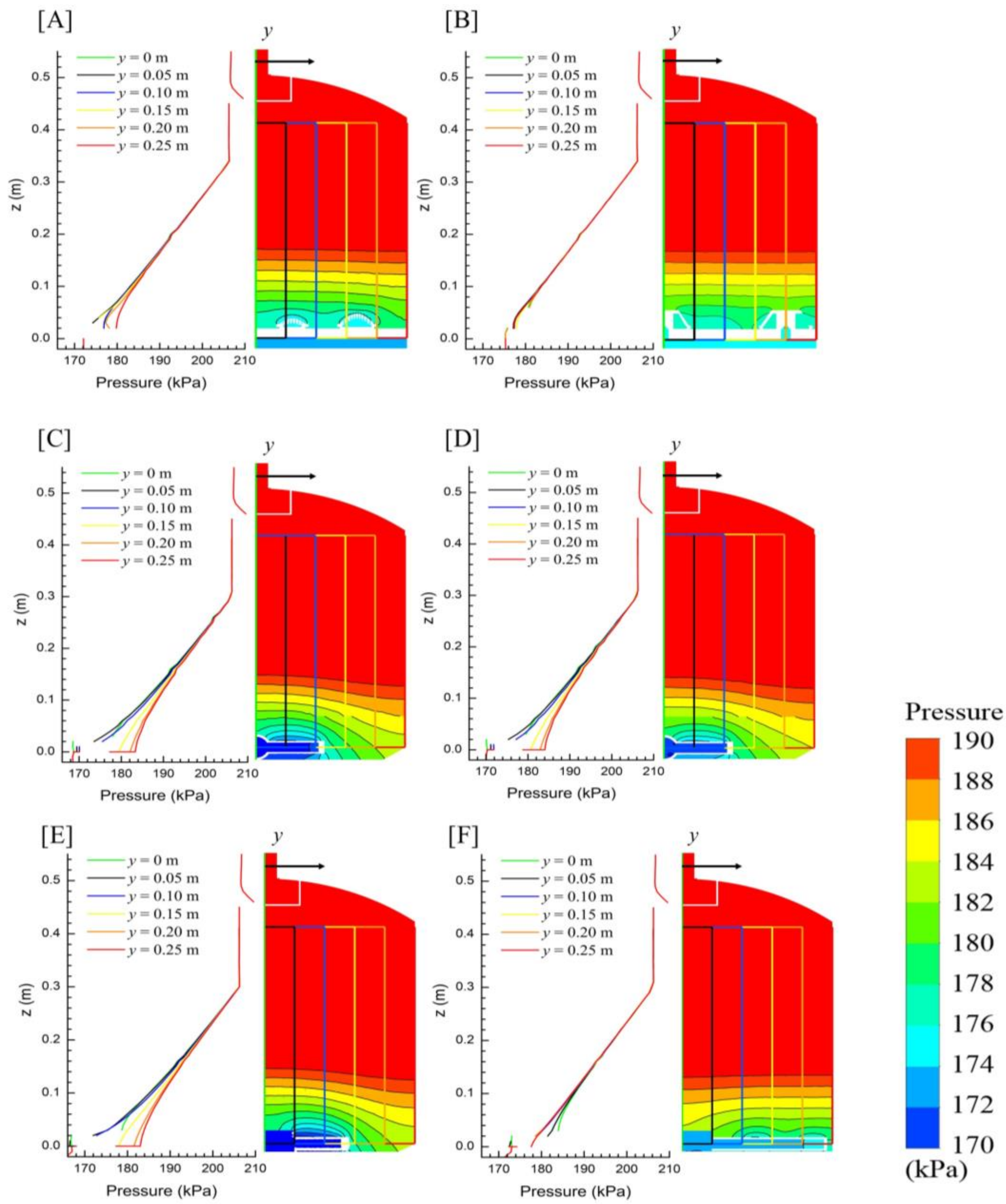

Fig. 10 – Pressure values along different lines shown at plane $x = 0$ m where pressure contours for the 170-190 kPa range are also depicted. Cases correspond to P12 [A],P19 [B], Wa [C], Wb [D], Sa [E], Sb [F] filter designs with operational conditions $H_s = 300$ mm and $Q = 12$ m^3 h^{-1}.

The effect of the underdrain for the P12 pod-type design was very remarkable below $z = 0.06$ m since pressure variations of almost 8 kPa were observed between points in the sand region at the same height. Indeed, changes in the slope of the pressure profile along the investigated paths were already obtained below $z = 0.2$ m (Fig. 10A). Pressure contour lines clearly deviated from the horizontal as they were near the pod underdrain. On the contrary, this behaviour was not detected for the P19 case, in which all of pressure vertical profiles analysed behaved almost equally (Fig. 10B). The P19 had an increase of 58% of the total slot open area A_o as well as of the area covered value A_c with respect to the P12 case (Table 1). Although the coefficient of variation for both P12 and P19 was similar (0.10 and 0.11, respectively), the behaviour was different since the flow inside the granular bed for the P19 was much more uniform than in the P12 distribution. In comparison with the other pod-type designs here analysed, the increase of the slot open area of the P19 case reduced the flow velocity within the sand media near the underdrain. This fact decreased the head losses in that region. In addition, the increase of the total underdrain exit area also reduced both primary and minor hydraulic losses when clean water flowed through the pod to the bottom chamber.

Pressure local vertical profiles as well as pressure contour results were very similar for both wand-type Wa and Wb configurations at plane *x* = 0 m (Fig. 10C-D). Note the important curvature of the pressure contour lines as they approached the wand. These surfaces of constant pressure inside the media tended to be perpendicular to the streamlines. Since these underdrain designs concentrated the slots in a narrow region at the filter centre, water from the outer regions of the filter flowed almost radially towards the slots at low *z* values (see the highly inclined contour pressure lines in Fig. 10C-D). The effect of the underdrain clearly modified the slope of the pressure local vertical profiles at locations $z < 0.22$ m.

The results for the spike-type Sa and Sb configurations substantially differed (Fig. 10E-F). The pressure field for case Sa was very similar to those previously found for wand-types Wa and Wb, with contour pressure lines substantially affected by the underdrain in regions distant from the slots (Fig. 10E). However, the Sb design, although with the same slot open area than Sa, provided quite a uniform flow behaviour, with almost horizontal pressure contours all the way till the underdrain (Fig. 10F). In this case, the vertical pressure profile along different lines almost matched until $z = 0.1$ m, below which slight differences between them were found. Therefore, this smooth behaviour of the pressure field in the Sb design provided low pressure losses, being below those found for the P12 case.

3.1.4 to the filter pressure drop

The contribution of filter accessories (diffuser plate and collector) to the overall filter pressure drop was estimated from the $\Delta p_{f,w}/\Delta p_f$ ratio where $\Delta p_{f,w}$ was the pressure drop of the filter when working empty of sand media (Burt, 2010). These ratios varied from 8% to 30% depending on the operational conditions and filter designs (Fig. 12). For a fixed value of the superficial velocity, the highest $\Delta p_{f,w}/\Delta p_f$ ratio was found for the smallest amount of sand (lowest H_s values), as expected. On the other hand, for a fixed amount of sand, the $\Delta p_{f,w}/\Delta p_f$ ratio increased when increasing the flow rate. This occurred because head losses in the auxiliary elements were proportional to the square of the flow velocity (primary and minor hydraulic losses in turbulent flow), whereas head losses within the sand media were linear with the velocity (Eq. (3) with $C_2 = 0$). For $H_s =$ 300 mm and $Q = 12$ m^3 h^{-1} working conditions, the auxiliary filter elements, excluding external flushing valves, accounted for 18% (P19) or 20% (P12) of the total filter pressure drop. Lower values of $\Delta p_{f,w}/\Delta p_f$ were found for wand- and spike-type underdrain designs. This was a consequence of the high value of pressure drop obtained in the sand media for Wa, Wb and Sa cases and, hence, of the high Δp_f reached. However, the Sb case had a moderate pressure drop in the sand media, with a behaviour similar to that obtained for pod-type designs.

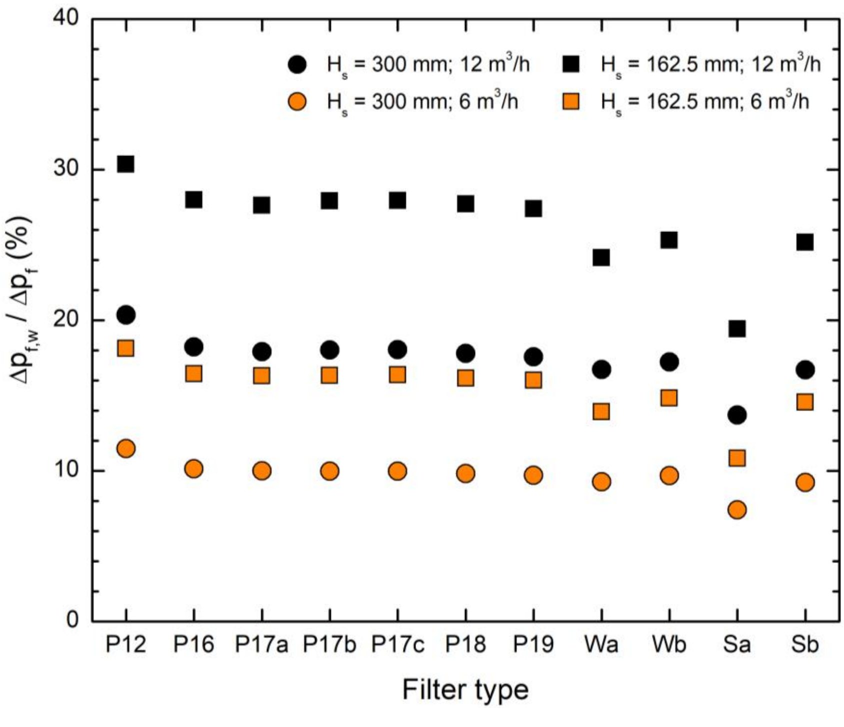

Fig. 12 – Ratio of filter pressure drop obtained with a filter empty of sand and a filter with a sand height equal to H_s.

The influence of auxiliary elements deduced by the $\Delta p_{f,w}/\Delta p_f$ ratio was confirmed from simulated data. All filter designs were divided into four regions of study. Region I consisted of the only-water region at the upper zone, from the inlet to the upper layer of sand medium. Region II took into account the sand medium, from the upper layer of sand medium to the slots of the underdrain system. Region III was the only-water region from the slots of the underdrain system to the exit of water of the underdrain elements into either the collector pipe (wand- and spike-types) or the bottom chamber (pod-type). Finally, region IV corresponded to the collector pipe or bottom chamber, being the zone comprised between the exit of the underdrain element and the exit of the filter. Pressure drop for each one of these four regions were obtained by subtracting the area averaged value of pressure at the surfaces that delimited them. For the $H_s = 300$ mm and $Q = 12$ m^3 h^{-1}, for example, we observed that the pressure drop at the inlet zone (region I), was very similar for all cases, being on the order of 0.50 kPa only (see Fig. 13). Almost the same values were obtained by Mesquita et al. (2019) in the analysis of several diffuser plate designs in a pressurised sand media filter.

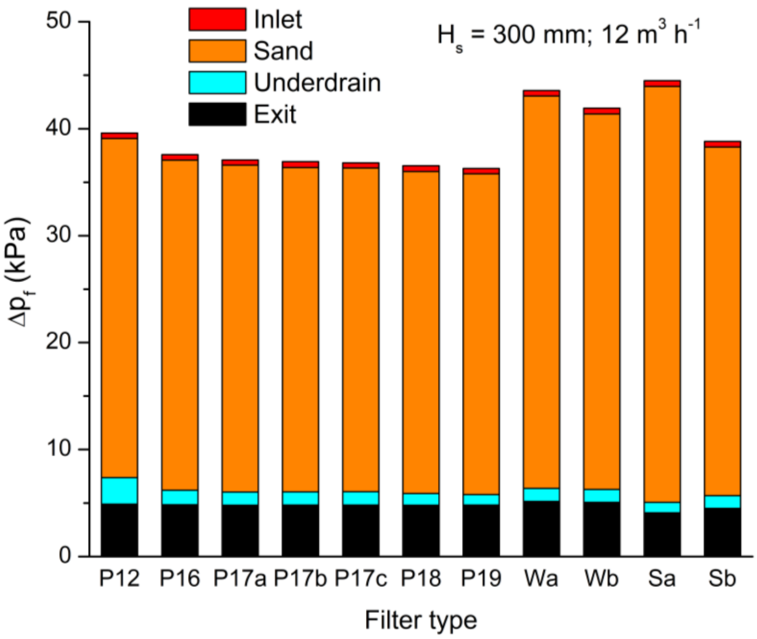

Fig. 13 – Pressure drop obtained in four regions of the filter. Conditions H_s = 300 mm and Q = 12 m^3 h^{-1}.

The pressure drop in the granular bed was maximum for the Sa type filter due to the high concentration of streamlines as the flow approached the slots inside the sand (see Fig.

11A). For the same reason, high values of the pressure drop were also reported for wand-type designs (Fig. 10A-B). Head losses of clean water flowing through the underdrain (pod, wand or spike) were especially high in the pod-type design P12 (2.46 kPa; $H_s =$ 300 mm and $Q = 12$ m^3 h^{-1} conditions). This value approximately decreased to 1.35 kPa for the P16 design, to 1.20 kPa for all the P17 designs, to 1.10 kPa for the P18 design and to 1.00 kPa for the P19 one. The inner configuration of the pod intensified the hydraulic minor losses, especially at the P12 where more flow rate per pod was required. In comparison, the pressure drop through wands was, approximately, 1.20 kPa, being similar to that for the Sb case (Fig. 13). The pressure drop for region IV was 4.90 kPa approximately for all pod-type designs, increasing to 5.10 kPa for the horizontal collector pipe in wand-type underdrains, and reducing to 4.50 kPa for the vertical central pipe in spike-type designs (Fig. 13; $H_s = 300$ mm and $Q = 12$ m^3 h^{-1} conditions). Thus, the pod-type design based on the commercial filter (P12) behaved the worst one in terms of head losses solely due to the underdrain.

The complex inner geometry of pods, with a cross-sectional exit area smaller than the slot open area implied the existence of intense water jets emerging into the lower chamber, particularly for the $Q = 12$ m^3 h^{-1} conditions in the P12 design (Fig. 14). In comparison, this high momentum jet was not observed in other configurations that directly discharged into a collector (see Fig. 14C). The local effect of the slots on the flow was also observed from the deviation of the velocity vectors near the underdrains (Fig. 14).

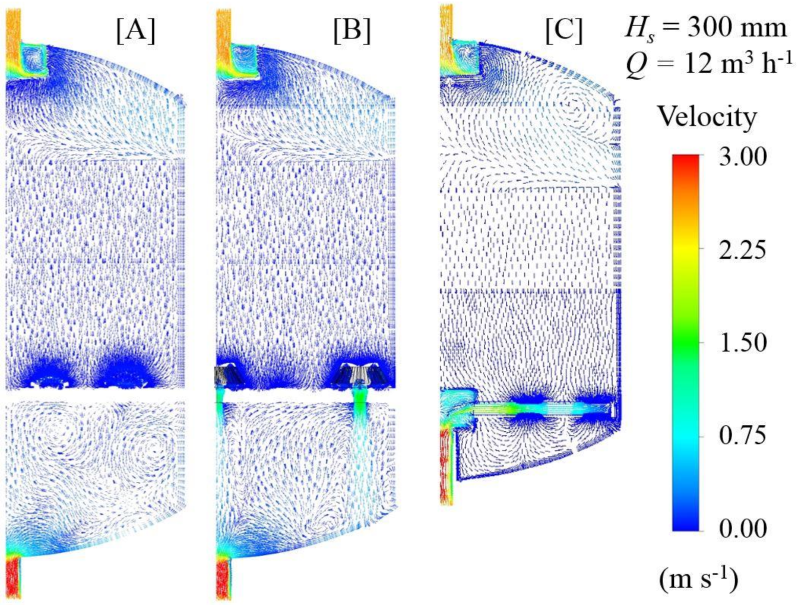

Fig. 14 – Velocity vectors at planes in Fig. 9 for the [A] P12 and [B] P19 cases and at plane in Fig. 11B, for the [C] Sa filter designs. Conditions H_s = 300 mm and Q = 12 m^3 h^{-1}.

The influence of the underdrain on the uniformity of the flow within the sand medium was analysed by dividing the cross-sectional area of the filter in ten equal areas (one inner circle and nine annular rings). The inner circle was identified as A1, whereas the annular rings were listed as A2 to A10, with A10 being the annulus that ended at the wall of the filter. We calculated the net flow through each one of these A1-A10 equal areas at intervals of 0.05 m of height within the granular bed (see Fig. 15). Thus, results at z = 0.05 m in Fig. 15 were only calculated using the flow obtained in the sand domain although at this height the xy-plane also contained some only-water regions inside the pods.

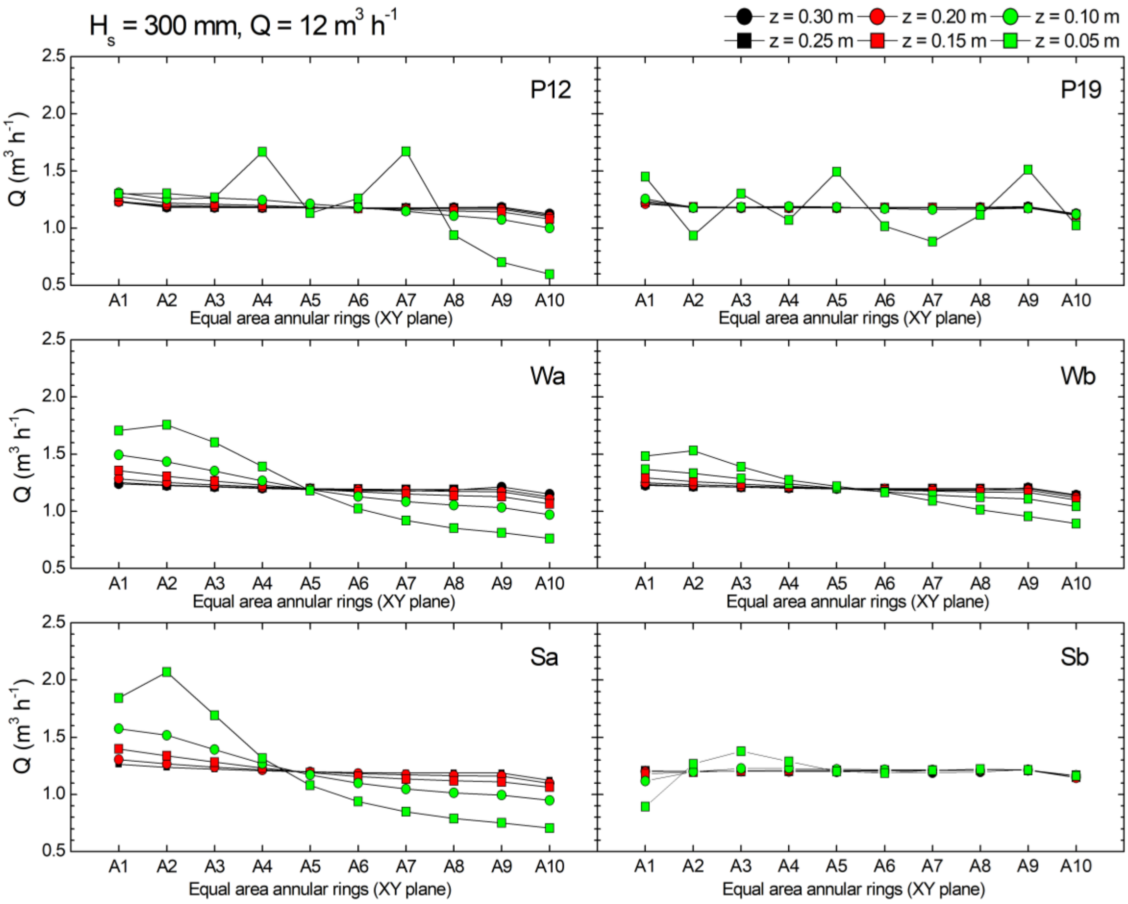

Fig. 15 – Flow rate through sand medium in 10 horizontal equal areas located at the xy-plane for different heights z. A1 is an inner circular area with an origin at the filter centre. A2 to A10 are annular areas, with A10 the most external one. Conditions H_s = 300 mm and Q = 12 m^3 h^{-1}.

In general, the contribution of the outer annular ring (A10) was lower than other regions due to the effect of the no-slip boundary there. Note that the uniformity of the flow within the sand for the pod-type designs was very high, especially for the P19 design in which data from z = 0.30 m to z = 0.10 m coincided (Fig. 15). Differences were observed near the underdrains (z = 0.05 m) with peaks of flow in those three radial regions where underdrains were located (see Fig. 3). For the P12 configuration, differences in uniformity were more evident as we moved closer to the underdrain. At z = 0.05 m, there were two peaks only, since in this pattern, pods were distributed in two radial distances only (no central pod unit was installed, see Fig. 3). We noted the low flow rate obtained through the external annulus. In comparison, both wand-type designs here analysed behaved similarly. The behaviour was much more uniform closer to the wands than in the pod-type designs, without showing the picky performance near the underdrain element. The flow rate decreased from the most internal annular area to the most external one for both Wa and Wb cases, being more uniform for the latter design. This behaviour was also observed in the spike-type design Sa. However, the modified design Sb clearly exhibited a better performance in terms of flow uniformity, with very low deviations, even at z = 0.05 m (Fig. 15), being only relevant near the centre since that area was not covered by slots (see Fig. 3).

Figure 15 was developed to determine the flow uniformity within the sand medium. The variability of the flow per underdrain element was also investigated by summing up the volumetric flow through the slots per each individual underdrain element. We carried out a basic descriptive statistical analysis for these data series and plotted the normalised deviations from the mean flow per slot in a box plot that included the median (horizontal line shared by boxes), the first and third quartile (upper and lower limit of boxes) and the minimum and maximum values (end of whiskers) (Fig. 16). In Fig. 16, Q_i corresponded to the flow through the i-th underdrain element and $Q_{mean} = \sum_{i=1}^{N} Q_i/N$ with N the number of underdrain elements (e.g., 12 for P12, 16 for P16, …, 19 for P19 and 10 for Wa, Wb, Sa and Sb; see Fig. 3). Data of Fig. 16 were obtained for the $H_s = 300$ mm and $Q = 12$ m^3 h^{-1} working conditions. As expected from Fig. 3, spikes in Sa and Sb configurations exhibited a very high uniformity of flow values. This contrasted with the wand-type design, in which the commercial configuration Wa reached the highest variability of all the cases here analysed. The modified wand-type design with equal served area per underdrain substantially reduced the flow variations between wands, as already pointed out in Pujol et al. (2020). Pod-type designs also suffered of high variability, especially those configurations with a pod in the centre of the filter. This central pod had the minimum flow value in Fig. 16 for P16, P17a-c, P18 and P19 cases. Note also that case P17c had a very low flow variability between underdrain elements, with a very reduced interquartile range. In comparison, designs with the same number of pods but differently distributed (P17a-b) clearly showed an uneven flow circulation, being configurations that produced a higher pressure drop than (P17c) (see Fig. 6). Indeed, the P17c case had the lowest c_v value (Table 1).

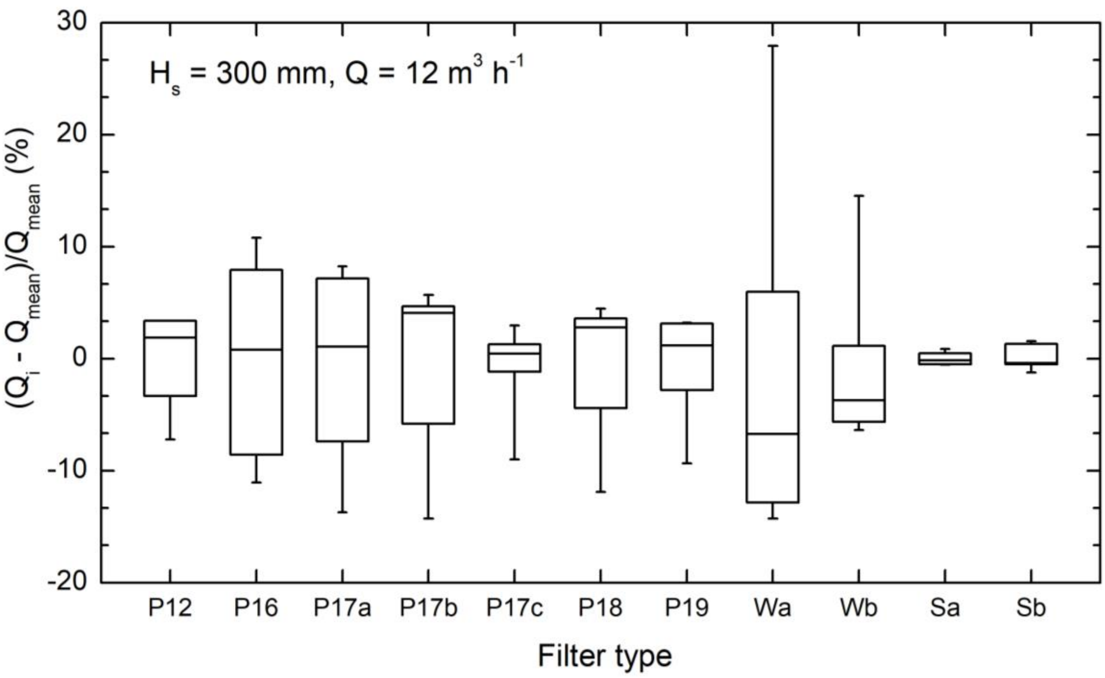

Fig. 16 – Median (centre line), quartile 1 and 3 (boxes) and minimum and maximum (end of whiskers) values of volumetric flow data series (with respect to the mean value) per each individual underdrain element. Conditions H_s = 300 mm and Q = 12 m^3 h^{-1}.

3.2. Backwash mode

Finally, the pressure drop through the filter in the backwashing mode was represented in Fig. 17. No sand was considered since the possibility of having a fluidized bed was not possible with the model setup here defined. However, the comparison between filters of the pressure drop obtained with only water conditions might be useful to assess their performance relative to each other when including the sand medium. Results indicated that the commercial design P12 had a slightly higher pressure drop than the spike-type design Sb. Of course, adding pods in the filter decreased the backwashing pressure loss, reaching a minimum for the P19 configuration. Wand-type configuration revealed as very appropriate for the backwashing mode, with remarkable low values of the pressure drop for both of the flow rate tested (Fig. 17).

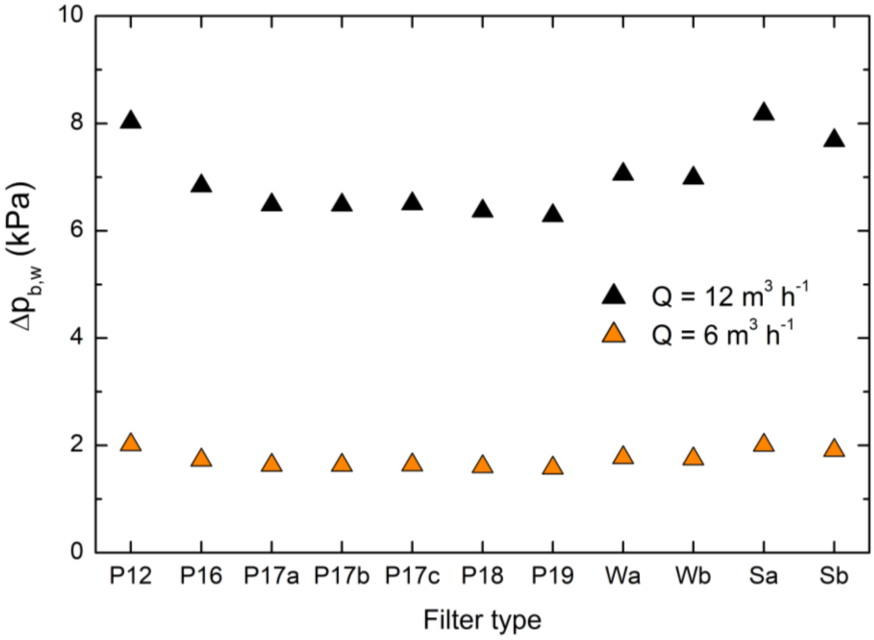

Fig. 17 – Pressure drop in backwashing mode for only water conditions.

4. Conclusions

We carried out a numerical study of 11 underdrain designs in a pressurized sand media filter. These designs were divided into three categories depending on the underdrain element used: pod (7 designs), wand (2 designs) and spike (2 designs). Models that resembled available commercial filters were P12 (12 pods) and Wa (wand, type a). Wb (wand, type b), Sa and Sb (spike-types) models were not far from some market designs. Pod-type models from P16 to P19 would be difficult to commercialize due to the cost of using such a high number of individual underdrain elements. However, these configurations were analysed since they had values of the slot open area similar than those of wand- and spike-type filters.

All filters had the same inner diameter and had the same diffuser plate. All were tested with the same conditions of flow rate (6 and 12 m^3 h^{-1}) and sand column height (162.5 and 300 mm). A reference ideal case with a slot open area equal to the cross-sectional area of the filter was also simulated. In comparison with this ideal case, the commercial pod-type P12 design for the high flow conditions (superficial velocity equal to 61.1 m h^{-1}) had a filter pressure drop 12% higher. The spike-type case Sb for the same conditions produced a lower filter pressure drop than the P12 case.

An increase in the number of pods reduced the overall filter pressure drop, essentially by two effects: 1) it increased the flow uniformity in the sand medium (i.e., the pressure drop in the sand region was lower); 2) it decreased the flow rate per underdrain element (i.e., the hydraulic losses through the underdrain element were lower). For a fixed number of pods, the distribution of the underdrain units on the base plate also affected the flow uniformity and, hence, the pressure drop. For the P17 case, a redistribution of the pods in order to achieve a better coefficient of variation reduced the pressure drop in 1.4% for the 30.6 m h^{-1} superficial velocity and 162.5 mm sand height case.

In conditions with 61.1 m h^{-1} superficial velocity and 300 mm sand height (excluding the effect of flushing valves), the sand medium was responsible of 82-87% of the total filter pressure drop. The pressure losses through the underdrain reached 6% of the total value for the P12 case, but reducing to 3% in wand- and spike-type configurations. The hydraulic losses in the bottom chamber (pod-type) or collector (wand- and spike-type designs) accounted for 9-13% of the total pressure drop. For all cases, the pressure drop at the inlet region, including the effect of the diffuser plate, was the less important contribution, being below 2%. However, the diffuser plate is a key element of the filter in order to slow down and to redirect the flow inside the filter so as to become as uniform as possible when entering the sand region.

Results revealed that the variability of the flow rate between individual underdrain elements reduced the efficiency of the system. The central pod was not always recommended since it may favour the hydraulic imbalance with the rest of the pods. In backwashing mode with only water conditions, the spike-type designs had lower pressure losses than commercial type P12 case, although the best configuration for these operational conditions was that with wands. Thus, from the results obtained, the spike-type design with large coverage zones (Sb) was comparable, and even better, than the commercial P12 case.

Acknowledgements

The authors would like to express their gratitude to Spanish Research Agency and the European Regional Development Fund for their financial support through Grant RTI2018-094798-B-100.

References

ANSYS, Inc. (2017). ANSYS Fluent User's Guide. Canonsburg, PA, USA: ANSYS Inc.

Arbat, G., Pujol, T., Puig-Bargués, J., Duran-Ros, M., Barragán, J., Montoro, L. & Ramírez de Cartagena, F. (2011). Using computational fluid dynamics to predict head losses in the auxiliary elements of a microirrigation sand filter. Transactions of the ASABE, 54(4), 1367 -1376.

Arbat, G., Pujol, T., Puig-Bargués, J., Duran-Ros, M., Montoro, L., Barragán, J. & Ramírez de Cartagena, F. (2013). An experimental and analytical study to analyze hydraulic behavior of nozzle-type underdrains in porous media filters. Agricultural Water Management, 126, 64-74.

Bové, J., Arbat, G., Pujol, T., Duran-Ros, M., Ramírez de Cartagena, F., Velayos, J., & Puig-Bargués, J. (2015a). Reducing energy requirements for sand filtration in microirrigation: improving the underdrain and packing. Biosystems Engineering, 140, 67–78.

Bové, J., Arbat, G., Duran-Ros, Pujol, T., M., Velayos, J., Ramírez de Cartagena, F., & Puig-Bargués, J. (2015b). Pressure drop across sand and recycled glass media used in micro irrigation filters. Biosystems Engineering, 137, 55–63.

Bové, J., Puig-Bargués, J., Arbat, G., Duran-Ros, M., Pujol, T., Pujol, J., & Ramírez de Cartagena, F. (2017). Development of a new underdrain for improving the efficiency of microirrigation sand media filters. Agricultural Water Management, 179, 296-305.

Burt, C. (2010). Hydraulics of commercial sand media filter tank used for agricultural drip irrigation. ITCR Report No. R 10001. San Luis Obispo, CA, USA: Irrigation Training and Research Center.

de Deus, F.P., Mesquita, M., Salcedo Ramirez, J.C., Testezlaf, R., & de Almeida, R.C. (2020) Hydraulic characterisation of the backwash process in sand filters used in micro irrigation. Biosystems Engineering, 192, 188-198.

Mesquita, M., Testezlaf, R. & Ramirez, J. (2012). The effect of media bed characteristics and internal auxiliary elements on sand filter head loss. Agricultural Water Management, 115, 178-185.

Mesquita, M., de Deus, F.P., Testezlaf, R., da Rosa, L.M., & Diotto, A.V. (2019). Design and hydrodynamic performance testing of a new pressure sand filter diffuser plate using numerical simulation. Biosystems Engineering, 183, 58-69.

Nakayama, F. S., Boman, B. J., & Pitts, D. J. (2007). Maintenance. In F.R.Lamm, F.R., J.E.Ayars, & F.S.Nakayama. (Eds.), Microirrigation for Crop Production (pp.389-430). Amsterdam: Elsevier.

Ojha, C.S.P., & Graham, H.J.D. (1994). Computer-aided simulation of slow sand filter performance. Water Research, 28 (5), 1025-1030.

Pujol, T., Arbat, G., Bové, J., Puig-Bargués, J., Duran-Ros, M., Velayos, J., & Ramírez de Cartagena, F. (2016). Effects of the underdrain design on the pressure drop in sand filters. Biosystems Engineering, 150, 1-9.

Pujol, T., Puig-Bargués, J., Arbat, G., Duran-Ros, M., Solé-Torres, C., Pujol, J., & Ramírez de Cartagena, F. (2020). Effect of wand-type underdrains on the hydraulic performance of pressurised sand media filters. Biosystems Engineering, 192, 176-187.

Solé-Torres, C., Puig-Bargués, J., Duran-Ros, M., Arbat, G., Pujol, J. & Ramírez de Cartagena, F. (2019). Effect of underdrain design, media height and filtration velocity on the performance of microirrigation sand filters using reclaimed effluents. Biosystems Engineering, 187, 292-304.

Solé-Torres, C. (2020). Underdrain design and operational conditions in sand media filters using reclaimed effluents in drip irrigation systems. PhD dissertation, University of Girona, Girona.